Materials Today Communications 39 (2024) 108892

Contents lists available at ScienceDirect

Materials Today Communications

journal homepage: www.elsevier.com/locate/mtcomm

Modeling of time-dependent mechanical behavior of oleic acid nanocomposites using nanoindentation

V. Kolli [a,*], I. Scheider [a], H. Ovri [b], D. Giuntini [c,e], C. Cyron [a,d]

[a] Helmholtz Zentrum Hereon, Institute for Material Systems Modeling, Max–Planck-Straße 1, Geesthacht, 21502, Schleswig - Holstein, Germany
[b] Helmholtz Zentrum Hereon, Institute for Hydrogen Technology, Max–Planck-Straße 1, Geesthacht, 21502, Schleswig - Holstein, Germany
[c] Hamburg University of Technology, Institute of Advanced Ceramics, Denickestraße 15, Hamburg, 21073, Germany
[d] Hamburg University of Technology, Institute for Continuum and Material Mechanics, Eißendorfer Str. 42 (Geb. M), Hamburg, 21073, Germany
[e] Eindhoven University of Technology, Department of Mechanical Engineering, De Rondom 70, Eindhoven, 5612 AP, Netherlands

ARTICLE INFO

Keywords:
Nanocomposites
Superlattices
Nanoindentation
Creep
Material modeling
Parameter identification

ABSTRACT

Supercrystalline nanocomposites are a burgeoning class of hybrid inorganic–organic materials. Studies showed that self-assembly of iron oxide particles surface-functionalized with organic (e.g. oleic acid) ligands produces a supercrystalline nanocomposite with exceptional mechanical properties. Consequently, significant research has been conducted on these materials to experimentally characterize the mechanical properties of such materials. However, so far all modeling studies used time and rate independent elastoplastic material models. In the light of new experimental results, we propose to extent this view and use time-dependent models to capture viscoelastic behavior. To this end, we quantified this behavior using nanoindentation creep experiments and modeled it using a rheological network model with several parallel Maxwell branches and an additional elasto-plastic branch. We demonstrate how the parameters of such a model can be found using inverse analysis. With the calibrated material model, a good agreement of the time dependent behavior between simulation and experimental results is achieved. Thus, a method is provided to model time dependent behavior using complex non-classical experiments like nanoindentation.

1. Introduction

In the realm of materials engineering, there has been an increasing focus on structurally-ordered nanocomposites in recent years [1,2]. These materials are integral to the creation of hierarchical materials systems that exhibit complex functionalities [3–6]. Termed as supercrystalline nanocomposites, these materials consist of inorganic nano building blocks that are typically surface-functionalized with organic ligands. They are organized into periodic arrangements, akin to crystalline structures, often referred to as superlattices. This new class of materials find applications in a wide variety of fields like friction coatings, energy storage, optoelectronics, catalysts and sensors etc. [7–11]. The fabrication and assembly of these sturdy supercrystalline inorganic–organic nanocomposites have emerged as key areas of interest in this rapidly evolving field [12]. Numerous strategies have been employed for the creation of self-assembled nanocomposites [9,13,14], resulting in a broad array of techniques and potential applications [15]. The mechanical properties exhibited by these materials significantly surpass those of hard polymers, and the consensus within the scientific community is that supercrystallinity by ligand cross-linking plays a vital role in augmenting the strength, hardness, and stiffness of the nanocomposites [16–20].

Initially, Dreyer et al. [21] demonstrated the fabrication of face-centered cubic supercrystalline nanocomposites composed of magnetite particles (Fe_3O_4), surface-functionalized with oleic acid. They were synthesized through a sequential process of sedimentation, drying, pressing, and heat treatment. The resulting nanocomposites displayed remarkable mechanical properties, particularly when heat treated at higher temperatures (325 °C), due to an increased degree of cross-linking.

To date, several material models have been employed in the simulation of this new class of materials, in particular the Drucker–Prager elastoplastic material model [22] and a nonlocal damage model based on micropolar continuum theory, which focused on the inelastic and damage behavior of the crosslinked organic interphase and was validated using experimental data from microbeam bending tests [23]. In a recent study [24], a non-linear elastic material model was used to capture the tension–compression asymmetry observed in pentagonal cross-sectioned micro-cantilever beam bending experiments. All these

* Corresponding author.
E-mail address: vasu.kolli@hereon.de (V. Kolli).

https://doi.org/10.1016/j.mtcomm.2024.108892
Received 6 January 2024; Received in revised form 28 March 2024; Accepted 9 April 2024
Available online 12 April 2024

models have in common that they can only capture the instantaneous (time-independent) material response. However, recent nanoindentation studies conducted by Yan et al. [25] have revealed that the material exhibits notable time-dependent behavior. The objective of the current study is to model this time-dependent behavior.

Modeling time-dependent material behavior for nanocomposites is challenging due to experimental limitations. Conventional creep characterization methods, including uniaxial creep testing, multiaxial creep testing, and stress relaxation testing, are not feasible for supercrystalline nanocomposites, due to their characteristic small sample sizes. Hence, suitable experimental approaches are restricted to nanoscale-mesoscale techniques, such as nanoindentation, microbeam bending and microcolumn compression etc. These methods, however, are intricate, as multiple material deformation mechanisms – including plasticity, microcracking, crack deflection, strain hardening, stress concentrations, and material compaction – may occur simultaneously [26–28]. This complexity makes it difficult to isolate and analyze the time-dependent behavior of the material. Given its relative simplicity in experimentation, nanoindentation has been selected as the experimental technique for the current study.

The investigation of material properties using indentation techniques has a long history, dating back to Hertz's work on elastic solids contact [29]. Later developments by Sneddon [30], Bulychev et al. [31], and Doerner and Nix [32] led to the extraction of elastic and plastic material behavior. Oliver and Pharr [33] further refined the method for determining hardness and Young's modulus through nanoindentation-based mechanical characterization. This contact-theory-based analytical approach has been modified and applied to characterize viscoelastic [34–37] and viscoelasto-plastic behavior [38–40]. Although this analytical method enables determination of properties such as reduced modulus, storage modulus, and viscous coefficient from nanoindentation tests, reliability is influenced by various assumptions and correction factors, and importantly complex material behavior laws remain inaccessible through this analytical approach. Hence, alternative iterative methods have been proposed to characterize material properties by combining contact theory and finite element methods (FEMs). One such method is inverse analysis.

The inverse analysis method uses an optimization algorithm and numerous nanoindentation FEM simulations to find the best-fit material parameters for a specific material model. The method inversely fits FEM simulation results to the experiments by systematically varying the material parameters. The quality of the solution depends on the optimization algorithm, initial point, how the "best-fit" is defined and calculated (i.e. error function), and stopping criterion for the iterations. The method was first introduced by Kavanaugh and Clough [41] to characterize non-linear elastic materials, by representing strain energy function as a power series. Subsequently many studies have successfully used this method to extract material parameters for elasto-plastic [42–47], viscoelastic (plastic) [48–53], and viscoelastic-viscoplastic [54,55] material models by mainly using nanoindentation force displacement ($P - h$) curves, in some cases complemented with residual indent measurements. It is already well known that the inclusion of residual indent data improves the accuracy of inferred material parameters [44]. The Burgers model (linear and non-linear) [51,56–58], Kelvin-Voigt model [57,59,60], generalized Maxwell's model [61], and standard linear solid model [62] are the most prominent models used for modeling viscoelasticity.

In this paper, we propose a generalized Maxwell's model (implemented as a parallel rheological framework (PRF) in Abaqus® [63]) to capture the viscoelastic properties of supercrystalline nanocomposites formed by self assembly of inorganic iron oxide nanoparticles surface-functionalized with organic oleic acid and heat treated at 325 °C to induce crosslinking. This model supports non-linear viscoelasticity in combination with plasticity. It allows considerable variations by varying the number of viscoelastic branches and the associated flow rules to model the nanoindentation experiments. Our study aims at understanding and modeling time-dependent material behavior of oleic acid nanocomposites. To this end, the material samples are prepared (Section 2), nanoindentation creep experiments were conducted (Section 3) and also simulated using the finite element method (FEM) with the Abaqus® PRF material model (Section 4). The material model parameters were extracted using inverse analysis (Section 4). The results of the parameter identification are presented and discussed (Section 5).

2. Material processing and microstructure

The material was developed by Institute of Advanced Ceramics at Hamburg University of Technology as part of a collaborative project SFB986 - Tailor made multi-scale material systems. The material is composed of iron oxide (Fe_3O_4 nanoparticles, coated with oleic acid ($C_{18}H_{34}O_2$, 11% wt.), and is synthesized by CAN GmbH (Hamburg, Germany). Initially, the surface functinalized nanoparticles are dispersed in toluene and this emulsion is transformed into supercrystalline bulk pellets through a three-step process: self-assembly, compression, and heat treatment [21]. For sample preparation, the toluene suspension containing the nanoparticles is placed into molds, and then exposed to an ethanol-rich atmosphere in a sealed container for 15 days, allowing for self-assembly. After this period, the solvent is removed, and the samples are dried under vacuum. The dried materials, consisting of supercrystalline grains in a face-centered cubic arrangement, are pressed into cylindrical pellets. This pressing is done uniaxially at 50 MPa and 150 °C. The pressed samples undergo a final heat treatment. This treatment is conducted under nitrogen gas at 325 °C for 18 min, with controlled heating and cooling rates. This comprehensive process yields supercrystalline materials with superior mechanical properties. According to previously conducted experimental investigations [26–28], these nanocomposites possess an experimentally determined Young's modulus E of approximately 50 GPa, a bending strength of around 630 MPa, a hardness of 4.7 GPa, and a fracture toughness of 0.5 MPa$\sqrt{m}$, thus showing predominantly brittle material behavior. However, recent nanoindentation experiments showed lower Young's modulii at higher indentation depths, namely 22 GPa at 2 μm and 16 GPa at 7.5 μm [64]. This discrepency will be discussed in detail later in Section 3.2.

The studied FCC supercrystalline material consist of iron oxide (magnetite, Fe_3O_4) spherical nanoparticles with a radius of 7.9 ± 1.3 nm and surface functionalized with oleic acid. Small-angle X-ray scattering (SAXS) analysis reveals these supercrystals exhibit a lattice constant of approximately 24.5 nm, implying an organic material-filled interparticle distance of about 1.5 nm within the densely arranged ⟨110⟩ directions.

Although the nanocomposites show remarkable mechanical properties, thanks to the cross-linking of the organic phase, fabrication of supercrystalline nanocomposites in macroscopic scale leads to the development of a very broad set of superlattice defects, ranging from point defects (interstitials and vacancies) to line (dislocations), surface/interface (grain boundaries), and volume defects (pores and cracks). The presence of numerous defects in bulk macroscopic samples fabricated by self-assembly has already been well documented in the literature [16,65]. The Fig. 1 shows examples of superlattice defects, detected in virgin samples (i.e. no experiments were conducted on them after fabrication) showing that the defects formed during the fabrication. An additional source of imperfections is the unavoidable size scatter of the constituent nanoparticles (a size scatter of > 20% often leads to "superamorphous" structures).

3. Experiments

3.1. Setup and loading

In many investigations, a Berkovich indenter is used for nanoindentation analysis to extract hardness, elastic modulus, fracture toughness etc. [33,66,67]. By contrast, we chose a spherical indenter for the current creep study for three reasons: Firstly, the indenter is not self

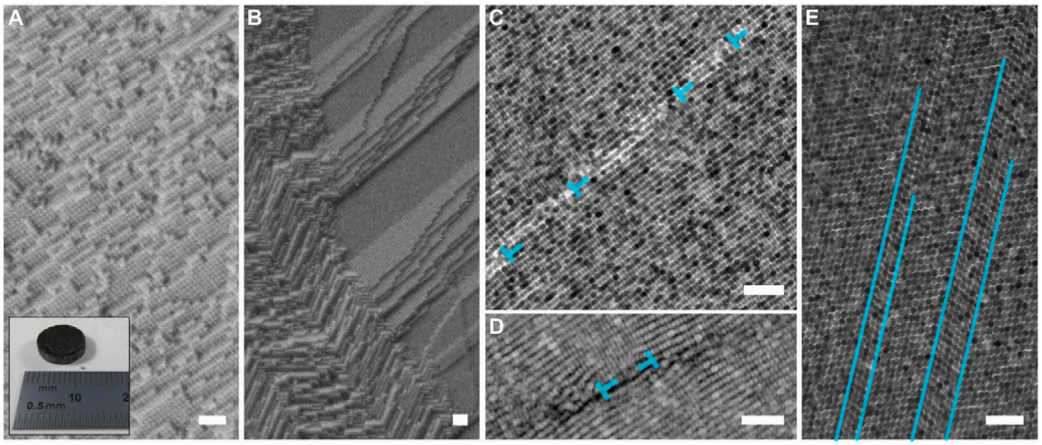

Fig. 1. Nanostructure and defects in bulk supercrystalline nanocomposite. (A) SEM image showing single supercrystal FCC nanostructure and bulk pellet after processing. (B) SEM image of supercrystalline interface (high-angle grain boundary). (C) TEM image of low-angle grain boundary. (D) STEM high-angle annular dark field micrograph of Frank partial. (E) TEM image of twins. All scale bars are 100 nm.
Source: Image taken from Giuntini et al. [28].

similar and hence the stress and strain fields change with indentation depth. This reduces the risk of obtaining very similar $P-h$ curves for different stress–strain relationships [68]. Commonly, self similarity is an advantage for parameter identification for experimental studies, but for numerical parameter identification it is beneficial to have different stress states at different indentation depths. Secondly, a spherical indenter simplifies the simulation model, as it can be represented as an axi-symmetric model. This helps in significantly reducing the computational costs of the parameter identification. Third, the objective of the current study is to extract homogenized bulk material properties. Hence it is important to probe the sample over a large area (several grains) with as little material compacting as possible due to stress concentrations (causing plastic hardening) especially during the initial stage of indentation. At any given indentation depth, a spherical indenter offers higher contact area than a Berkovich or cube corner indenter, produces uniform stress fields during the indentation process, and by choosing an indenter with a diameter of 10 μm it is assured that multiple grains are probed.

The nanoindentation tests were performed with a Nanoindenter XP (MTS Corp.) in continuous stiffness measurement (CSM) mode with a spherical indenter of diameter 10 μm. CSM is a mode of nanoindentation testing that allows for the continuous measurement of material properties such as dynamic contact stiffness, hardness etc. during the entire indentation process, unlike the standard mode where you can extract the material properties just once during unloading. By dynamically oscillating the indenter during loading, it provides several unloading states to measure the material properties, improving the accuracy of measurements and offering a more comprehensive understanding of the material's behavior under different loading conditions.

Each nanoindentation test consists of 5 phases as shown in Fig. 2:

1. Loading in CSM mode (amplitude 2 nm, frequency 45 Hz) at a specified indentation strain rate $\dot{\epsilon}_i$ up to a specified target depth h_t.
2. Holding the load at target depth h_t for 1500 s.
3. Unloading to 10% of the indenter load during hold time P_{hold}.
4. Machine enforced thermal drift correction phase for 500 s.
5. Complete unloading and resting.

The term indentation strain-rate $\dot{\epsilon}_i$ was first coined by Lucas and Oliver [69] and it can be described as follows:

$$\dot{\epsilon}_i = \frac{\dot{h}}{h} = \frac{1}{2}\left(\frac{\dot{P}}{P} - \frac{\dot{H}}{H}\right) \approx \frac{1}{2}\frac{\dot{P}}{P} \tag{1}$$

where h is indentation depth, P is indentation load, and H is indentation hardness.

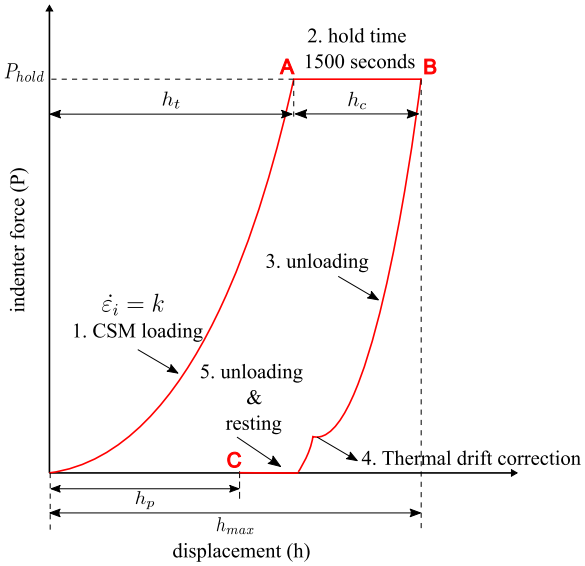

Fig. 2. Load v/s displacement curve of a nanoindentation test showing different phases, where h_t is target depth, P_{hold} is force during phase 2, h_c is displacement during phase 2 (creep displacement), h_p is residual indent depth, h_{max} is maximum indentation depth, $\dot{\epsilon}_i$ is indentation strain-rate, and points A, B, C are points of interest for error calculation.

In a nanoindenter, the displacement is measured by using a three-plate capacitor, to which a shaft is attached with the tip at the bottom. Maintaining thermal stability in the instrument is crucial because small changes in the spacing between the capacitor plates can be mistakenly read as movement of the tip, leading to errors in depth measurements. This kind of error is known as thermal drift. Typically, thermal drift is measured before applying any load or at 10% of the maximum load during unloading. Corrections are then made to negate the impact of thermal drift. In the current CSM loading profile, the measurement of thermal drift at 10% of the maximum load during unloading is automatically included by the machine, lasting for a period of 500 s, and this is seen in phase 4 of the current nanoindentation tests. However, it is already well documented that this conventional method of thermal drift measurement does not work well for long-duration measurements, like creep and high-temperature experiments [70–73]. Hence, in the current study thermal drift measurement (and subsequently correction) is performed using the method proposed by Maier et al. [74]. The method is based on the use of dynamic contact stiffness S_{csm} obtained

Table 1
Nanoindentation experimental results showing average values of Young's modulus E, hold force P_{hold}, final residual indent h_p and creep displacement h_c.

Load case (Name - $\dot{\varepsilon}_i$ - h_t)	Experimental Young's modulus E [GPa]	Hold force P_{hold} [mN]	Residualindent h_p [nm]	Creep displacement h_c [nm]
LC1 - 0.5/s–1600 nm	36	177	849	612
LC2 - 0.05/s–1600 nm	42	158	737	678
LC3 - 0.05/s–1400 nm	41	141	583	496
LC4 - 0.05/s–1200 nm	40	112	434	539
LC5 - 0.005/s–1400 nm	27	98	404	178

by CSM, to minimize thermal drift. This allows for reliable creep data to be obtained from nanoindentation creep experiments even at enhanced temperatures and for duration up to 10 h. The method involves continuously recording the dynamic contact stiffness during the indentation test by using the CSM mode. While the indentation depth recorded by the system is highly influenced by thermal drift, the contact stiffness is not, allowing the true contact area to be reliably determined using Sneddon's equation [75], provided the reduced modulus E_r of the material is known. The actual indentation depth is then calculated from the contact area using tip area function and finally, the actual indenter displacement is obtained after sink-in corrections are made.

A total of 5 experimental load cases (LCs) with 10 indents each, were conducted and the load case parameters were as follows:

- Load case 1 (LC1): Strain rate $\dot{\varepsilon}_i = 0.5/\text{s}$, target depth $h_t = 1600$ nm.
- Load case 2 (LC2): Strain rate $\dot{\varepsilon}_i = 0.05/\text{s}$, target depth $h_t = 1600$ nm.
- Load case 3 (LC3): Strain rate $\dot{\varepsilon}_i = 0.05/\text{s}$, target depth $h_t = 1400$ nm.
- Load case 4 (LC4): Strain rate $\dot{\varepsilon}_i = 0.05/\text{s}$, target depth $h_t = 1200$ nm.
- Load case 5 (LC5): Strain rate $\dot{\varepsilon}_i = 0.005/\text{s}$, target depth $h_t = 1400$ nm.

In each load case, indentations were performed in a single row, maintaining a consistent distance of 30 μm between any two consecutive indents.

In this study, cross-sectional analyses of the three nanoindents per load case are performed to measure the residual depths. A focused gallium Ga^+ ion beam (FIB) in an FEI Nova 200 dual beam FIB/SEM microscope is used to mill through the mid-section of the nanoindents, enabling precise depth measurements. To protect the sample surface during the milling process, a 1 μm-thick platinum layer is deposited across the mid-section of the indents prior to cross-sectioning. A representative cross-section of one of the indents after milling is depicted in Fig. 3a, b.

3.2. Experimental results and discussion

Upon examining the experimental displacement history curves (Fig. 4), a significant amount of experimental scatter was observed, as illustrated exemplarily in Fig. 4 for one load case. The experimental data scatter arises from the large variety of defects present in these nanocomposites. These defects can be (1) Processing-induced – due the unavoidable nanoparticle size scatter (variation in particle size > 20%) & various superlattice defects (Fig. 1) and the large scale of the self-assembly process; and (2) Indentation-induced – due to the variety of cracks formed during nanoindentation (Fig. 3c, d) in this predominantly brittle material.

Considering the significant uncertainty of experimental results, averages have been calculated for residual indent values h_p, hold force P_{hold} and displacement during phase 2 (creep displacement) h_c, Young's modulus E calculated during phase 1, and tabulated in Table 1. It should be noted that the reported residual indent values average at least three residual indentation tests per load case.

The elastic modulus E obtained from the current nanoindentation experiments is significantly lower than the estimates reported in previous studies [21,24–27]. This discrepancy can be attributed to process and nanoindentation defects discussed earlier (Section 2) which is typical of organic–inorganic nanocomposite supercrystals [76,77]. Other factors such as indenter type and indenter size effects based on indentation depth could also come into play [78]. Most of the previous studies [21,24–27] used Berkovich indenter instead of spherical indenter and they did not indent to a depth of 2.5 μm like in the current study. This could also explain lower experimental Young's modulus E values in the current study when compared to previous studies.

Additionally, the experimentally measured Young's modulus E during CSM loading via nanoindentation shows an inconsistency in its rate-dependency. Typically, an increase of E with strain rate is expected (given that the material is granted less time for viscoelastic relaxation). This trend holds except for an outlier, load case 1. Intriguingly, the E value corresponding to a strain rate of $0.5/\text{s}$ is actually lower than that at $0.05/\text{s}$, defying the expected behavior. This could be due to the same factors that caused the experimental scatter.

As anticipated, the hold load P_{hold} increases with indentation depth for a constant indentation strain rate (Table 1). This observation aligns with the expectation that higher forces are necessary to achieve greater indentation depths. Consequently, at a fixed target depth, the hold force increases with the indentation strain rate, which can be attributed to the material's viscosity or rate dependency. The residual indent depth consistently increases as the hold force rises. In contrast to these observations, the creep displacement did not show any clear dependence on Young's modulus E, indentation strain rate $\dot{\varepsilon}_i$, target depth h_t or hold load P_{hold}.

4. Modeling

4.1. Material model

The generalized Maxwell model used in this study was developed by J.A. Hurtado and I. Lapczyk [79] and implemented in the commercial finite element software Abaqus® [63] as parallel rheological framework (PRF). It has been used successfully to describe the mechanical behavior of a number of filled rubbers and polymers [80,81]. The framework consists of an arbitrary number N of parallel viscoelastic branches (Fig. 5). In addition, a purely elastic or elasto-platic equilibrium branch, typically referred to as branch 0, can be added. The addition of plasticity to the equilibrium branch allows for modeling permanent set, in the present case residual indent.

The material response is always assumed to be isotropic. Both plasticity and creep are assumed to be volume preserving (isochoric). For each of the branches, the deformation gradient $\mathbf{F}$ is split into an elastic part (superscript 'e') and an inelastic part due to creep (superscript 'cr') or plasticity (superscript 'pl'):

$$\begin{aligned} \mathbf{F} &= \mathbf{F}_i^e \mathbf{F}_i^{cr} \quad i = 1, \ldots, N \\ \mathbf{F} &= \mathbf{F}_0^e \mathbf{F}_0^{pl} \end{aligned} \tag{2}$$

The total strain energy W_T is equal to the weighted sum of strain energies W^i of all branches:

$$W_T = \sum_{i=0}^{N} s_i W^i \left(\mathbf{C}_i^e\right) \tag{3}$$

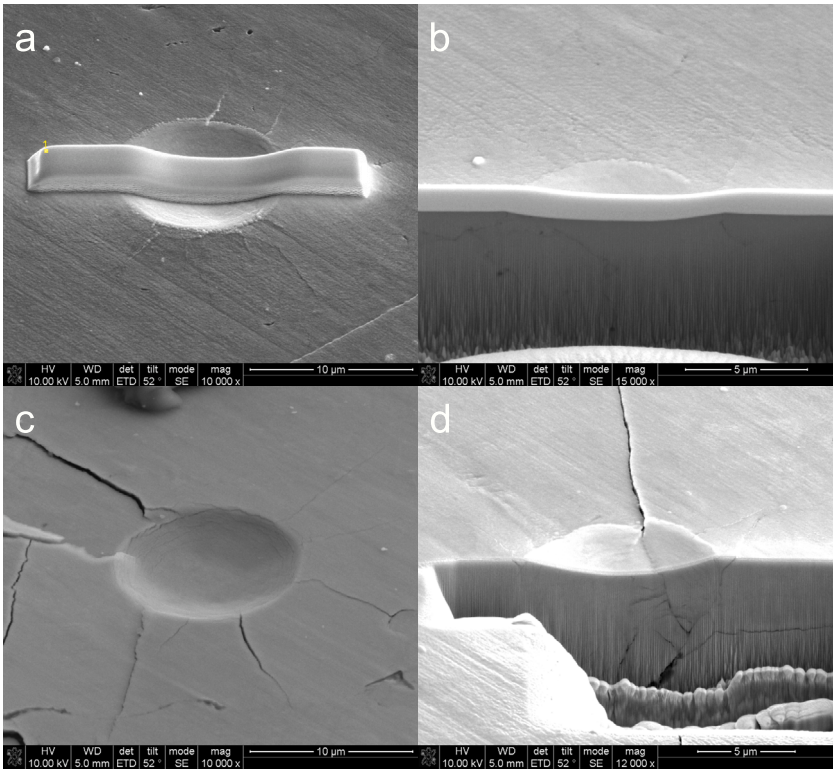

Fig. 3. (a) Sample of a residual indent with platinum layer before milling, (b) Cross-section of an indent after milling, (c) Cracks after indentation for an indent, and (d) Cracks under an indent after milling.

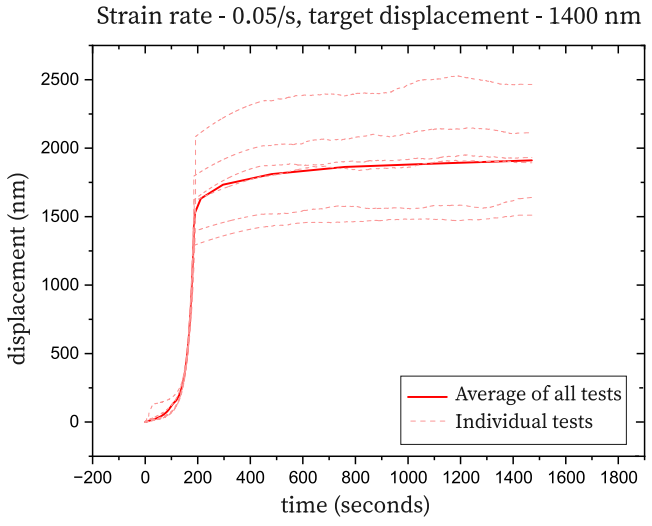

Fig. 4. Experimental displacement history curves with large scatter band for the load case with indentation strain rate $\dot{\epsilon}_i = 0.05/\text{s}$ and target depth = 1400 nm.

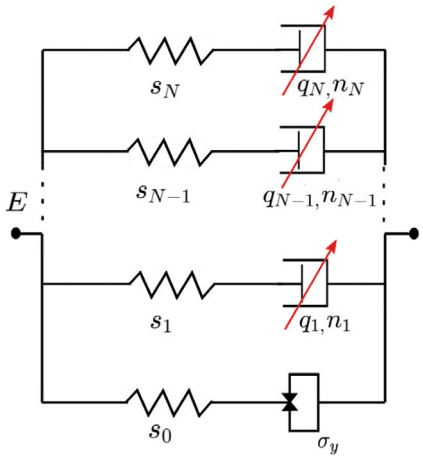

Fig. 5. Abaqus® - Parallel Rheological Framework consisting of N viscoelastic branches and a single elastoplastic branch (also called the equilibrium branch), with relevant material parameters. Here, E is Young's modulus, s_i is stiffness ratios (weights), σ_y is yield strength, and q_i, n_i are creep law parameters.

with weights s_i (stiffness ratios) forming a partition of unity, i.e., $\sum_{i=0}^{N} s_i = 1.0$. The total stress response thus becomes

$$\boldsymbol{\tau} = \sum_{i=0}^{N} s_i \left\{ \mathbf{F}_i^e \cdot 2 \frac{\partial W\left(\mathbf{C}_i^e\right)}{\partial \mathbf{C}_i^e} \cdot \left(\mathbf{F}_i^e\right)^T \right\} = \sum_{i=0}^{N} s_i \boldsymbol{\tau}_i \tag{4}$$

where $\boldsymbol{\tau}$ is the total Kirchhoff stress tensor, and $\boldsymbol{\tau}_i$ is Kirchhoff stress tensor of branch i. The plastic response of the equilibrium branch 0 is formulated as the multiplicative split of the deformation gradient containing elastic and plastic parts as shown below.

$$\dot{\mathbf{F}}^{pl} = \mathbf{F}^{e^{-1}} \cdot \mathbf{D}^{pl} \cdot \mathbf{F}^{e} \cdot \mathbf{F}^{pl} \tag{5}$$

where the plastic deformation rate $\mathbf{D}^{pl}$ is given by the associated flow rule

$$\mathbf{D}^{pl} = \frac{3}{2q} \dot{\bar{\epsilon}}^{pl} \overline{\boldsymbol{\tau}} = \dot{\bar{\epsilon}}^{pl} \mathbf{n} \tag{6}$$

of the von Mises yield condition and

$$q - \tau^y(\bar{\epsilon}^{pl}) = 0. \tag{7}$$

Here, q is the effective Kirchhoff stress $q = \sqrt{\frac{3}{2}\overline{\boldsymbol{\tau}} : \overline{\boldsymbol{\tau}}}$, where $\overline{\boldsymbol{\tau}}$ is the deviatoric part of the Kirchhoff stress tensor, and τ^y is the non-linear

work hardening function which depends on the so-called equivalent plastic strain $\bar{\varepsilon}^{pl}$.

The evolution of the creep part of the deformation gradient for any branch $i > 0$ is given by

$$\dot{\mathbf{F}}_i^{cr} = \mathbf{F}_i^{e^{-1}} \cdot \mathbf{D}_i^{cr} \cdot \mathbf{F}_i^{e} \cdot \mathbf{F}_i^{cr} \tag{8}$$

where $\mathbf{D}_i^{cr}$ the creep part of the deformation gradient for any branch $i > 0$, which can be given by

$$\mathbf{D}_i^{cr} = \frac{3}{2\tilde{q}_i} \dot{\bar{\varepsilon}}_i^{cr} \bar{\boldsymbol{\tau}}_i \tag{9}$$

with $\dot{\bar{\varepsilon}}_i^{cr}$ the equivalent creep strain rate, $\bar{\boldsymbol{\tau}}_i$ the deviatoric part of the Kirchhoff stress tensor for a branch $i > 0$, and $\tilde{q}_i = \sqrt{\frac{3}{2}\bar{\boldsymbol{\tau}}_i : \bar{\boldsymbol{\tau}}_i}$. To keep the number of parameters in the inverse analysis small, a rather simple power law model was used in the current study, represented as follows:

$$\dot{\bar{\varepsilon}}_i^{cr} = \left(\frac{\tilde{q}_i}{q_i}\right)^{n_i} \tag{10}$$

where q_i, n_i are material parameters to be determined for each branch i.

In the current study, two PRF models were employed:

Material model 1PRF: PRF model consisting of one viscoelastic branch and one elastoplastic branch, and

Material model 2PRF: PRF model comprising two viscoelastic branches and one elastoplastic branch.

The material parameters to be determined through inverse analysis are Young's modulus E, stiffness ratios s_i, yield strength σ_y, stress constants q_i, and stress exponents n_i, where $i = 1, 2, \ldots, N$, and N denotes the number of viscoelastic branches. Therefore, the material model 1PRF has five material parameters: E, s_1, σ_y, q_1, n_1. In contrast, the material model 2PRF has eight parameters: E, s_1, s_2, σ_y, q_1, n_1, q_2, n_2. The parameter s_0 can be computed by $s_0 = 1 - \sum_{i=1}^{N} s_i$. It is also important to note that the Poisson's ratio ν is assumed to be 0.3. Additionally, the brittleness and compaction of the material are not considered in the current model.

4.2. Finite element model

An axisymmetric finite element model was built using the commercial software Abaqus®. The specimen was modeled as a deformable body and meshed with linear triangular (Abaqus® designation CAX3) and quadrilateral (CAX4) elements. The indenter was modeled as a rigid surface. A gradient mesh where the mesh size increases with distance from the indenter was employed (Fig. 8a). A sensitivity analysis confirmed that this mesh was sufficiently fine to achieve a nearly converged solution, numerical stability, and largely mesh-independent results. A general frictionless surface-to-surface contact is defined between the deformable body and the rigid indenter. It is assured that a reasonable friction value ($\mu_F \leq 0.1$) does not alter the results significantly. Appropriate contact stabilization is used to deal with single-point contact that happens at the beginning of the simulation. Again, it has been checked that the influence on the simulation results is negligible.

The bottom of the deformable body is fixed and appropriate axisymmetric boundary conditions are applied along the edges. The experimental loading history is specified as a boundary condition on the indenter. Once the indentation is complete, the indenter is removed and the bulk material is allowed to rest for a very long time (10^8 s ≈ 3 years) to dissipate the viscous effects. The indentation depth recorded at the end of rest time is denoted as residual indentation, h_p, since the rate at that time displacement is less than machine accuracy, no further relaxation can be calculated. The displacement history of the indenter during the indentation and residual indent after the rest time are the outputs of the simulation, as they are dependent on the input material parameters.

4.3. Parameter identification through inverse analysis

The parameters for the PRF material model are determined from an inverse problem-solving approach henceforth called inverse analysis. The flowchart of this approach is shown in Fig. 6. The inverse analysis starts with an initial guess of the material parameters. A nanoindentation simulation with boundary conditions replicating real nanoindentation experiments is performed. The simulated displacement histories are then compared with experimental displacement histories and the error is calculated using an error function. If the error satisfies a defined stopping criterion, the parameters are accepted as the optimized material parameters, else another iteration is performed. To this end, the algorithm takes a 'step' in the parameter space using the Nelder Mead algorithm and uses an updated set of material parameters for the next iteration. This iterative process continues until the error value meets the stopping criterion. The effectiveness of the inverse analysis depends on the following factors:

- Optimization algorithm
- Error function and stopping criterion
- Initial parameter set

4.3.1. Optimization algorithm

Various optimization algorithms have been proposed so far. Global optimization schemes like simulated annealing algorithms (e.g., dual annealing, evolutionary algorithms like differential evolution, etc.) are computationally expensive but often the best choice if there is no prior information about the location of the solution in the parametric space. However, in the current scenario where each finite element simulation takes between 5–10 min, global optimization schemes are on one hand practically infeasible due to their high computational costs. At the same time, mechanistic insights into the physics of the system allow at least some confinement of the region in the parameter space where the optimal solution is likely located. In such cases, local optimization algorithms are typically a good choice. Unfortunately, the widely used class of gradient-based local optimization algorithms is not suitable here because of the high computational cost of calculating the Hessian of the error function. Among the many non-gradient local optimization algorithms, the Nelder–Mead optimization algorithm has been proven suitable for this application. Various previous studies [82–86] have successfully used this algorithm for parameter identification using nanoindentation albeit for other material models.

4.3.2. Error function and stopping criterion

The error function $\bar{e}(h^s)$ at any given time t is defined by a piecewise continuous linear function as shown in Fig. 7. Within the experimental scatter band (i.e. pink area in Fig. 7) the error is equal to absolute value of the relative error of the simulation from the experimental curve given by $|\frac{h^e - h^s}{h^e}|$ where h^e and h^s are experimental and simulated displacements at the same time t. By contrast, outside the experimental scatter band, the error is calculated by a line with slope of $\frac{\pm 100}{h^e}$ indicating that the error increases steeply when the simulation leaves the desired experimental scatter band.

The error function $\bar{e}(h^s)$ at any given time t is defined as

$$\bar{e}(h^s) = \begin{cases} \dfrac{100(h_O^e - h^s) + h_L^e}{h_O^e}, & \text{if } x < h_L^e \\ \dfrac{|h^s - h_O^e|}{h_O^e}, & \text{if } h_L^e \leq x \leq h_U^e \\ \dfrac{100(h^s - h_O^e) + h_U^e}{h_O^e}, & \text{if } x > h_U^e \end{cases} \tag{11}$$

where the superscripts e, s denote experiment and simulation, respectively, subscripts L, U, O denote lower bound, upper bound and

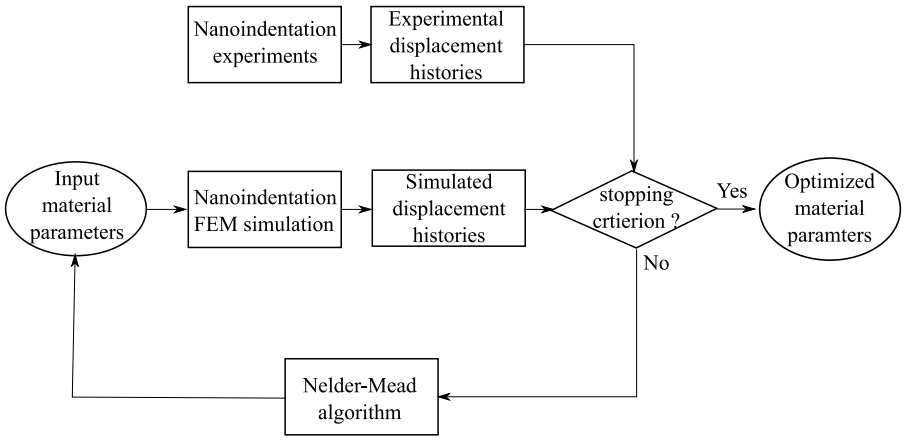

Fig. 6. Flow chart for inverse analysis.

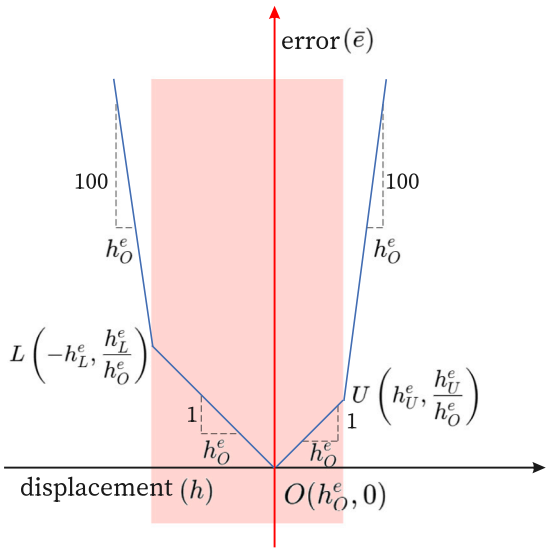

Fig. 7. Piece-wise continuous error function $\bar{e}(h_s)$ where the error increases much more steeply outside the experimental scatter (red) band than inside. Here, the superscript e, s denote experiment and simulation respectively, subscript L, U, O denote lower bound, upper bound and average of experimental scatter band respectively, and h is displacement.

average of experimental scatter band respectively, and h is displacement (indentation depth). The error for a load case is given by average of error function $\bar{e}$ values at points A, B and C as shown below

$$e = \frac{\bar{e}(h_A^s) + \bar{e}(h_B^s) + \bar{e}(h_C^s)}{3} \tag{12}$$

where h_A^s, h_B^s, h_C^s are simulated displacements at points A, B, C (see Fig. 2) respectively.

The error of a nanoindentation simulation is calculated by averaging the displacement error values at 3 different times: (1) the end of loading period (Point A in Fig. 2, displacement corresponding to h_t), (2) at the end of creep period (Point B, displacement h_{max}) and (3) at the total end time of residual indent calculation (10^8 seconds, Point C, displacement h_p).

The Nelder–Mead algorithm works by reflection and contraction of vertices of a simplex in the parametric space. When all possible transformations of a particular simplex did not improve the error by more than 10^{-5}, the iteration scheme was stopped and the minimum assumed to be reached.

4.3.3. Initial parameter set

The selection of an initial parameter set is critical for local optimization algorithms. These algorithms, including the Nelder–Mead algorithm, are susceptible to becoming trapped in a local optimum if the initial point is in proximity to a local optimum. Furthermore, a suitable initial point enhances convergence speed and algorithmic stability.

The average E during CSM loading for all load cases (Table 1) is 37.4 GPa. Additionally, microcantilever beam bending and micro-column compression tests [24] showed that the yield strength under compression is 1.2 ± 0.1 GPa. Hence the trust region for E and σ_y is set to be $[15, 40]$ GPa and $[700, 1300]$ MPa respectively.

As for the material parameters that determine time-dependent behavior, for the material model 1PRF, it turns out difficult to make initial guesses for the values of s_1 and q_1, necessitating a more expansive parametric space for these parameters. Based on commercial material model libraries like MCalibration [87], the parameter n_1 should lie for polymer composites between 3 and 8. In summary, the trust region for the material parameters of the 1PRF model is set as follows: $E \in [15, 40]$ GPa, $s_1 \in [0.1, 0.9]$, $q_1 \in [500, 10^4]$ MPa, $n_1 \in [3, 8]$, $\sigma_y \in [700, 1300]$ MPa.

For the material model 2PRF, defining a reasonable region in the parametric space is possible on the basis of the material model 1PRF parameters. The range for parameters shared with the 1PRF model is narrowed, as significant deviations are not expected. The new parameters q_2 and n_2 are anticipated to differ in magnitude from q_1 and n_1. Thus, their ranges are set as: $q_2 \in [10^4, 10^8]$ MPa, $n_2 \in [6, 12]$. The range of s_2 is set such that $\sum_{i=0}^{2} s_i = 1.0$.

Before the inverse analysis is performed, a sparse brute force evaluation of the error function is conducted throughout the whole above defined trust region within the parameter space. This evaluation is aimed to identify promising starting points with low error values, representing initial input material parameter sets for subsequent local optimization.

Finally, the inverse analysis is carried out using three load cases LC1, LC4 and LC5, to ensure that the effects of strain rate and target depth are captured. The load case LC3 is used for validation.

5. Computational results and discussion

5.1. Mesh sensitivity analysis

The effect of finite element size is investigated by simulating the same load case with identical material parameters while varying the element size. This mesh analysis is conducted using the LC1, as it can be expected to exhibit a particularly high mesh sensitivity due to the particularly high indentation depth and strain rate. The bulk material

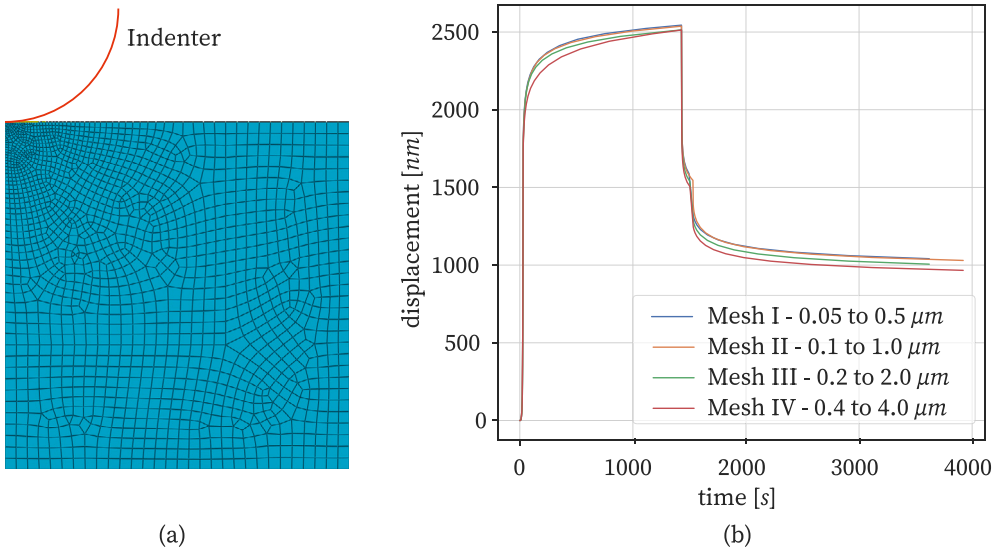

Fig. 8. (a) Indenter (simulated by a rigid contact boundary condition) and material sample meshed with optimal mesh (Mesh II) with element sizes varying from 0.1 to 1 μm, (b) Displacement history curves (till 3500 s) for different mesh sizes.

is meshed using a gradient mesh, wherein the element size increases with the distance from the indenter's first contact point (Fig. 8a). The displacement histories are compared for simulations with the following gradient meshes: Mesh I (0.05 to 0.5 μm), Mesh II (0.1 to 1 μm), Mesh III (0.2 to 2 μm), and Mesh IV (0.4 to 4 μm) (Fig. 8b).

It is crucial to examine the effect of element size on the displacement (indentation depth) at the end of the loading period (point A), the end of the creep period (point B), and the time of residual indent measurement (point C), as the displacements at these points are utilized to evaluate the error function. The average percentage change in displacement values at these points of interest (A, B, C) from Mesh IV to Mesh III is 1.34%. Similarly, the change from Mesh III to Mesh II is 1.43%, and from Mesh II to Mesh I, it is 0.38%. Therefore, we consider the solution obtained with Mesh II as sufficiently converged and thus an optimal trade-off between accuracy and computational cost. It has also been observed that, for Mesh II under LC1, the model's surface length is 5.26 times the contact length at point B. Although larger models have been shown to slightly alter the results, the size of the current model represents an optimal balance between accuracy and simulation time.

5.2. Material model 1PRF

When performing the local optimizations, a set of spatially close starting points was used to demonstrate convergence towards the same local minimum. The material parameters of the local minimum are summarized in the Table 2. The average error at the local minimum between the simulated displacements and the corresponding experimental displacements at points A, B, and C across the three load cases was found to be 8.2%. The displacement histories till the end of the creep period and displacement values of experiments and simulations are shown in Fig. 9, respectively.

Among the starting points explored, none were found to yield a lower error value than those presented in Table 2. This suggests that the identified local minimum may also be the global minimum. The simulations reached the residual indent position h_p after (on average) 33.26 days after the unloading and approximately 95% of the relaxation occurred within the first 20.32 h after unloading, as averaged across the three load cases.

5.3. Material model 2PRF

Similar to the material model 1PRF, the inverse analysis results using the material model 2PRF are tabulated in Table 2. The average error at the local minimum between the simulated and the corresponding experimental displacements at points A, B, and C across the three load cases was found to be 7.6%. The displacement histories till the end of creep period and displacement values of experiments and simulation at points A, B, C are shown in Fig. 9, respectively. On an average, it took approximately 5.68 h for the viscous effects to dissipate after the experiments to reach 95% of the simulated residual indent position, h_p. The final value h_p was reached after 7.79 days. Hence, the material model 2PRF reaches 95% of the simulated residual indent position 3.57 times faster than the model 1PRF, h_p was reached 4.26 times faster.

5.4. Validation

For model validation, we retained the data of the LC3. That is, these data were not used during the parameter fitting process and could thus not affect the values of the material parameters determined in this process. To study how the material models defined by these values generalize beyond the load cases used for the fitting process, we simulated with these material models the indentation process in case of the above defined validation load case. With the material model 1PRF and 2PRF, this yielded an average relative error between the experimental and simulated results of 11.16% and 10.8%, respectively. This demonstrates that our material model generalized well beyond the load cases used for the determination of the material parameters. The displacement histories for the experiments and simulations in the validation load case along with the displacements at points A, B, and C, are illustrated in Fig. 10.

5.5. Discussion

Both 1PRF and 2PRF material models exhibit a high yield strength of approximately 800 MPa, which agrees well with the findings of previous cantilever beam bending and microcolumn compression experiments [24].

Whereas the CSM mode of the nanoindenter provided on average the (instantaneous) Young's modulus of 37.4 GPa, our inverse analysis yielded (on average) 19.77 GPa. This discrepancy can likely be attributed to the inherent complexities and potential sources of error in nanoindentation experiments on viscoelastic materials. As outlined in the literature [88–91], nanoindentation tests for viscoelastic solids are fraught with issues including measurement of time constants, actuator dynamics, indenter size effects and inconsistencies between experimental conditions and modeling assumptions. These errors can be

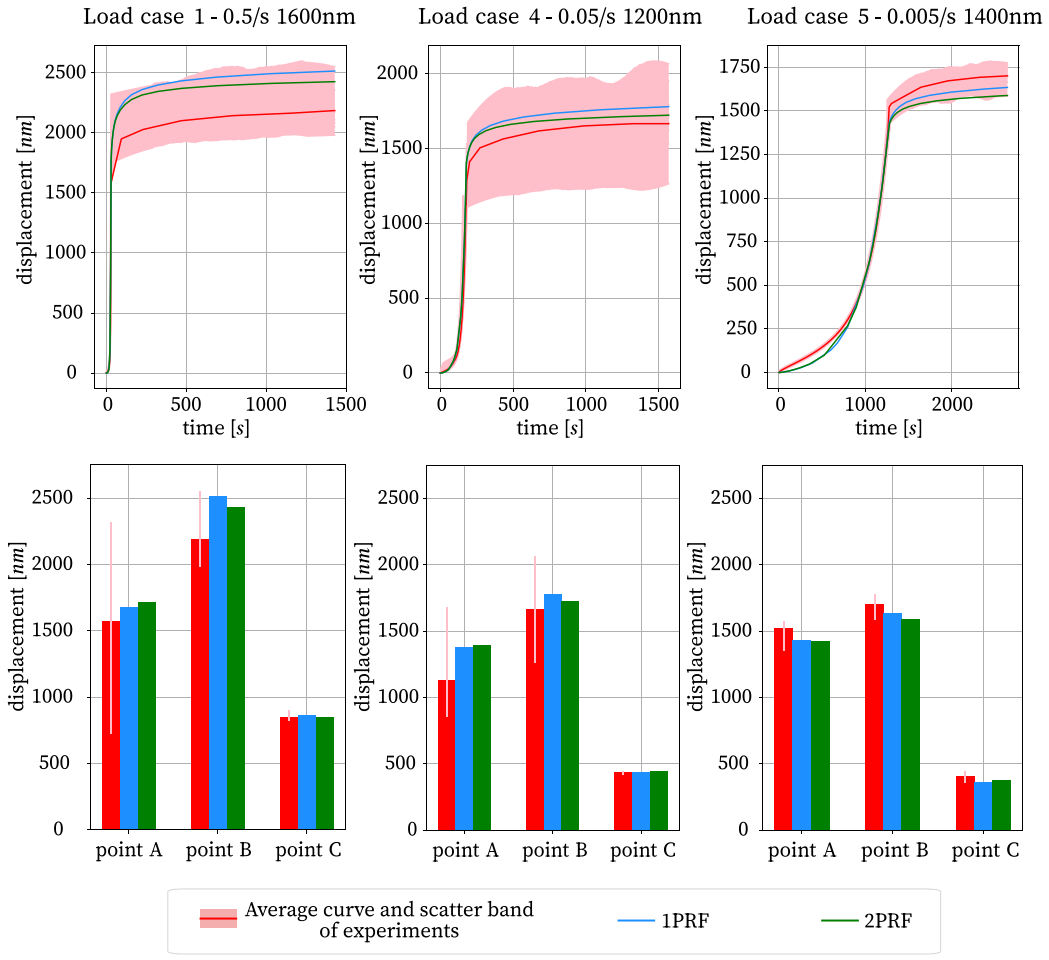

Fig. 9. Displacement histories and displacements at points A, B, C for material models 1PRF and 2PRF for material parameters shown in Table 2.

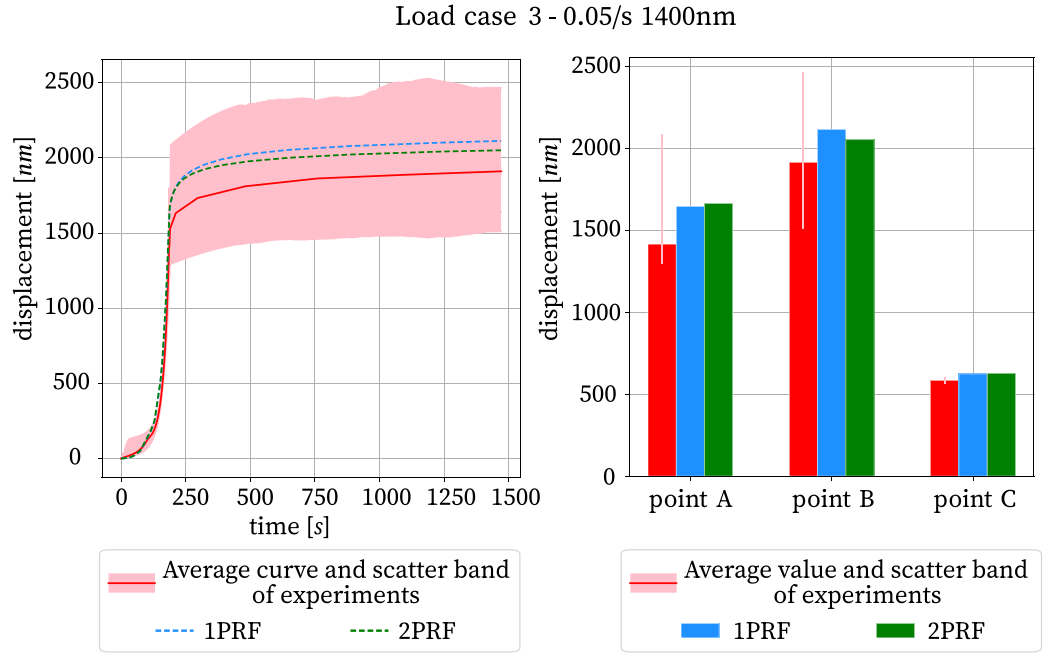

Fig. 10. Validation load case displacement histories (left) with experimental results and displacements at points A, B, C (right) for 1PRF and material model 2PRFs for material parameters shown in Table 2.

Table 2
Material model 1PRF, 2PRF parameters obtained from the inverse analysis.

Model	E [GPa]	s_1	q_1 [MPa]	n_1	s_2	q_2 [MPa]	n_2	σ_y [MPa]	Error (e) [%]
1PRF	20.8	0.66	1385	3.4	–	–	–	805	8.2%
2PRF	18.8	0.56	1489	3.0	0.023	2.31e5	7.8	771	7.6%

further amplified in small contact dimensions, where the outputs may be dominated by the measurement system itself. Generally, one can assume that the CSM-based calculation of Young's modulus is based on a less accurate mechanical model than our inverse analysis. Therefore, it appears reasonable to consider 19.77 GPa the more accurate and trustworthy value of Young's modulus.

Regarding the material time dependent behavior, the non-trivial value for s_1 shows that the material has significant time dependent behavior. The values of the stress exponent n_1, n_2 fall within the expected range for polymers $(3-8)$. However, these values are different from the previous nanoindentation creep study [25], because the current study calculates the stress exponent for the entire creep regime, as opposed to quasi-secondary creep regime, done in the previous study [25].

In our study, we compared two different generalized Maxwell models (1PRF with 5 parameters, 2PRF with 8 parameters) and the optimal material parameters of both resulting from the inverse analysis are in good agreement. This supports that the parameters of the model are representative of physical reality and not just rather random results of the solution of an ill-posed problem, which may sometimes happen in case of generalized Maxwell models with two many parallel branches.

6. Conclusions

In this study, the time-dependent behavior of supercrystalline nanocomposites, specifically those formed by the self-assembly of iron oxide particles surface-functionalized with organic oleic acid, was explored numerically using a continuum mechanics framework for the first time.

Initially, nanoindentation creep experiments are conducted using a spherical tip under 3 different loading strain rates and 3 different target indentation depths. These experiments are simulated using the finite element software Abaqus®. Two types of generalized Maxwell material models, referred to as 1PRF and 2PRF, were employed. They accounted for elastic–plastic behavior as well as for viscoelasticity with one and two parallel branches, respectively. This approach significantly goes beyond the simple Drucker–Prager elastoplastic material model used in previous studies. The parameters of our generalized Maxwell models were determined through inverse analysis, a method that proved effective in this context.

The inverse analysis was performed on three load cases and a fourth load case was used in the validation. The mean relative error between the simulated displacements and the corresponding experimental displacements at characteristic time points of the three load cases used for inverse analysis was found to be 8.2% and 7.6% for our two generalized Maxwell models, respectively. Using the parameters determined by this inverse analysis in the fourth (validation) load case yielded errors of 11.16% and 10.8% for the two material models, respectively. This confirms that the material models determined by our inverse analysis generalize well beyond the loading scenarios used for parameter fitting. Our analysis found creep stress exponents n_1, n_2 in the range between 3 and 8 and an instantaneous elastic modulus of $E = 19.77$ GPa. Note that this value is only around half as large as the one provided by CSM. The reason is likely the more accurate mechanical model underlying to our inverse analysis making the value of $E = 19.77$ GPa likely more trustworthy than the one that can be obtained with CSM.

Considerations must be made for the unique constraints of this study. Validation of the models under a broader range of experimental conditions with lesser experimental scatter is recommended. However, due to the small dimensions of the material samples used in this study, a more comprehensive range of experiments has not been feasible so far and may form an avenue of future research.

This study not only advances the understanding of supercrystalline oleic acid nanocomposites but also provides robust models for predicting their time-dependent behavior. For practical applications, ideally the current modeling methodology is more effective with lesser experimental scatter. The large experimental scatter in the current scenario affects the robustness of the material parameters. Finally, the current study forms the basis for modeling a second hierarchical level in the microstructure of these materials, which is the matter of our ongoing research.

CRediT authorship contribution statement

V. Kolli: Writing – original draft, Visualization, Validation, Software, Methodology, Investigation, Formal analysis, Data curation, Conceptualization. **I. Scheider:** Writing – review & editing, Resources, Project administration, Funding acquisition. **H. Ovri:** Writing – review & editing, Resources, Data curation. **D. Giuntini:** Writing – review & editing, Conceptualization. **C. Cyron:** Writing – review & editing, Funding acquisition.

Declaration of competing interest

The authors declare the following financial interests/personal relationships which may be considered as potential competing interests: Vasu Kolli reports financial support was provided by German Research Foundation. If there are other authors, they declare that they have no known competing financial interests or personal relationships that could have appeared to influence the work reported in this paper.

Data availability

Data will be made available on request.

Acknowledgments

This work was funded by the Deutsche Forschungsgemeinschaft (DFG, German Research Foundation) – SFB 986 – Project number 192 346 071. DG gratefully acknowledges the support of the Deutsche Forschungsgemeinschaft (DFG, German Research Foundation), project number GI 1471/1-1. VK and IS express their gratitude to Dr.-Ing. Jasmin Koldehoff and Cong Yan for their invaluable support with the nanoindentation experiments.

References

[1] S. Dhulipala, D.W. Yee, Z. Zhou, R. Sun, J.E. Andrade, R.J. Macfarlane, C.M. Portela, Tunable mechanical response of self-assembled nanoparticle superlattices, Nano Lett. 23 (11) (2023) 5155–5163, http://dx.doi.org/10.1021/acs.nanolett.3c01058.

[2] P.J. Santos, P.A. Gabrys, L.Z. Zornberg, M.S. Lee, R.J. Macfarlane, Macroscopic materials assembled from nanoparticle superlattices, Nature 591 (7851) (2021) 586–591, http://dx.doi.org/10.1038/s41586-021-03355-z.

[3] M. Mazzotti, A. Foehr, O. Bilal, A. Bergamini, F. Bosia, C. Daraio, N. Pugno, M. Miniaci, Bio-inspired non self-similar hierarchical elastic metamaterials, Int. J. Mech. Sci. 241 (2023) 107915, http://dx.doi.org/10.1016/j.ijmecsci.2022.107915.

[4] M. Miniaci, A. Krushynska, A.S. Gliozzi, N. Kherraz, F. Bosia, N.M. Pugno, Design and fabrication of bioinspired hierarchical dissipative elastic metamaterials, Phys. Rev. A 10 (2) (2018) http://dx.doi.org/10.1103/physrevapplied.10.024012.

[5] Z. Nie, A. Petukhova, E. Kumacheva, Properties and emerging applications of self-assembled structures made from inorganic nanoparticles, Nature Nanotechnol. 5 (1) (2009) 15–25, http://dx.doi.org/10.1038/nnano.2009.453.

[6] P. Fratzl, R. Weinkamer, Nature's hierarchical materials, Prog. Mater. Sci. 52 (8) (2007) 1263–1334, http://dx.doi.org/10.1016/j.pmatsci.2007.06.001.

[7] A.A. Voevodini, J.S. Zabinski, Load-adaptive crystalline–amorphous nanocomposites, J. Mater. Sci. 33 (2) (1998) 319–327, http://dx.doi.org/10.1023/a:1004307426887.

[8] C.S. Philip, A. Nivetha, C. Sakthivel, C. Veena, I. Prabha, Novel fabrication of cellulose sprinkled crystalline nanocomposites using economical fibrous sources: High performance, compatible catalytic and electrochemical properties, Microporous Mesop. Mater. 318 (2021) 111021, http://dx.doi.org/10.1016/j.micromeso.2021.111021.

[9] M.A. Boles, M. Engel, D.V. Talapin, Self-assembly of colloidal nanocrystals: From intricate structures to functional materials, Chem. Rev. 116 (18) (2016) 11220–11289, http://dx.doi.org/10.1021/acs.chemrev.6b00196.

[10] T. Tachikawa, T. Majima, Metal oxide mesocrystals with tailored structures and properties for energy conversion and storage applications, NPG Asia Mater. 6 (5) (2014) http://dx.doi.org/10.1038/am.2014.21, e100–e100.

[11] A.S. Baimuratov, I.D. Rukhlenko, V.K. Turkov, A.V. Baranov, A.V. Fedorov, Quantum-dot supercrystals for future nanophotonics, Sci. Rep. 3 (1) (2013) http://dx.doi.org/10.1038/srep01727.

[12] M.S. Lee, D.W. Yee, M. Ye, R.J. Macfarlane, Nanoparticle assembly as a materials development tool, J. Am. Chem. Soc. 144 (8) (2022) 3330–3346, http://dx.doi.org/10.1021/jacs.1c12335.

[13] B. Domènech, M. Kampferbeck, E. Larsson, T. Krekeler, B. Bor, D. Giuntini, M. Blankenburg, M. Ritter, M. Müller, T. Vossmeyer, H. Weller, G.A. Schneider, Hierarchical supercrystalline nanocomposites through the self-assembly of organically-modified ceramic nanoparticles, Sci. Rep. 9 (1) (2019) http://dx.doi.org/10.1038/s41598-019-39934-4.

[14] A. Plunkett, M. Kampferbeck, B. Bor, U. Sazama, T. Krekeler, L. Bekaert, H. Noei, D. Giuntini, M. Fröba, A. Stierle, H. Weller, T. Vossmeyer, G.A. Schneider, B. Domènech, Strengthening engineered nanocrystal three-dimensional superlattices via ligand conformation and reactivity, ACS Nano 16 (8) (2022) 11692–11707, http://dx.doi.org/10.1021/acsnano.2c01332.

[15] C. Sanchez, B. Julián, P. Belleville, M. Popall, Applications of hybrid organic–inorganic nanocomposites, J. Mater. Chem. 15 (35–36) (2005) 3559, http://dx.doi.org/10.1039/b509097k.

[16] E. Tam, P. Podsiadlo, E. Shevchenko, D.F. Ogletree, M.-P. Delplancke-Ogletree, P.D. Ashby, Mechanical properties of face-centered cubic supercrystals of nanocrystals, Nano Lett. 10 (7) (2010) 2363–2367, http://dx.doi.org/10.1021/nl1001313.

[17] P. Podsiadlo, G. Krylova, B. Lee, K. Critchley, D.J. Gosztola, D.V. Talapin, P.D. Ashby, E.V. Shevchenko, The role of order, nanocrystal size, and capping ligands in the collective mechanical response of three-dimensional nanocrystal solids, J. Am. Chem. Soc. 132 (26) (2010) 8953–8960, http://dx.doi.org/10.1021/ja100464a.

[18] P. Podsiadlo, B. Lee, V.B. Prakapenka, G.V. Krylova, R.D. Schaller, A. Demortiere, E.V. Shevchenko, High-pressure structural stability and elasticity of supercrystals self-assembled from nanocrystals, Nano Lett. 11 (2) (2011) 579–588, http://dx.doi.org/10.1021/nl103587u.

[19] M. Gauvin, N. Yang, Z. Yang, I. Arfaoui, M.-P. Pileni, Hierarchical mechanical behavior of cobalt supracrystals related to nanocrystallinity, Nano Res. 8 (11) (2015) 3480–3487, http://dx.doi.org/10.1007/s12274-015-0846-3.

[20] J. Wang, J. Schwenger, A. Ströbel, P. Feldner, P. Herre, S. Romeis, W. Peukert, B. Merle, N. Vogel, Mechanics of colloidal supraparticles under compression, Sci. Adv. 7 (42) (2021) eabj0954, http://dx.doi.org/10.1126/sciadv.abj0954.

[21] A. Dreyer, A. Feld, A. Kornowski, E.D. Yilmaz, H. Noei, A. Meyer, T. Krekeler, C. Jiao, A. Stierle, V. Abetz, H. Weller, G.A. Schneider, Organically linked iron oxide nanoparticle supercrystals with exceptional isotropic mechanical properties, Nature Mater. 15 (5) (2016) 522–528, http://dx.doi.org/10.1038/nmat4553.

[22] M. Li, I. Scheider, B. Bor, B. Domènech, G.A. Schneider, D. Giuntini, Ultra-thin and ultra-strong organic interphase in nanocomposites with supercrystalline particle arrangement: Mechanical behavior identification via multiscale numerical modeling, Compos. Sci. Technol. 198 (2020) 108283, http://dx.doi.org/10.1016/j.compscitech.2020.108283.

[23] S. Ma, I. Scheider, S. Bargmann, Ultrastrong nanocomposites with interphases: Non local deformation and damage behavior, Eur. J. Mech. A Solids 75 (2019) 93–108, http://dx.doi.org/10.1016/j.euromechsol.2019.01.011.

[24] B. Bor, D. Giuntini, B. Domènech, A. Plunkett, M. Kampferbeck, T. Vossmeyer, H. Weller, I. Scheider, G.A. Schneider, Constitutive and fracture behavior of ultra-strong supercrystalline nanocomposites, Appl. Phys. Rev. 8 (3) (2021) 031414, http://dx.doi.org/10.1063/5.0056616.

[25] C. Yan, B. Bor, A. Plunkett, B. Domènech, V. Maier-Kiener, D. Giuntini, Nanoindentation creep of supercrystalline nanocomposites, Mater. Des. 231 (2023) 112, http://dx.doi.org/10.1016/j.matdes.2023.112000.

[26] D. Giuntini, A. Davydok, M. Blankenburg, B. Domènech, B. Bor, M. Li, I. Scheider, C. Krywka, M. Müller, G.A. Schneider, Deformation behavior of cross-linked supercrystalline nanocomposites: An in situ SAXS/WAXS study during uniaxial compression, Nano Lett. 21 (7) (2021) 2891–2897, http://dx.doi.org/10.1021/acs.nanolett.0c05041.

[27] B. Bor, D. Giuntini, B. Domènech, M.V. Swain, G.A. Schneider, Nanoindentation-based study of the mechanical behavior of bulk supercrystalline ceramic-organic nanocomposites, J. Eur. Ceram. Soc. 39 (10) (2019) 3247–3256, http://dx.doi.org/10.1016/j.jeurceramsoc.2019.03.053.

[28] D. Giuntini, S. Zhao, T. Krekeler, M. Li, M. Blankenburg, B. Bor, G. Schaan, B. Domènech, M. Müller, I. Scheider, M. Ritter, G.A. Schneider, Defects and plasticity in ultrastrong supercrystalline nanocomposites, Sci. Adv. 7 (2) (2021) eabb6063, http://dx.doi.org/10.1126/sciadv.abb6063.

[29] H.R. Hertz, Über die berührung fester elastischer körper und über die härte, 2021, [Online; accessed 26. Nov. 2021] (No. 1881).

[30] I.N. Sneddon, The elastic stresses produced in a thick plate by the application of pressure to its free surfaces, Math. Proc. Cambridge Philos. Soc. 42 (3) (1946) 260–271, http://dx.doi.org/10.1017/S0305004100023021.

[31] S. Bulychev, V. Alekhin, M. Shorshorov, A. Ternovskii, G. Shnyrev, Determining young's modulus from the indentor penetration diagram, Ind. Lab. 41 (9) (1975) 1409–1412.

[32] M.F. Doerner, W.D. Nix, A method for interpreting the data from depth-sensing indentation instruments, J. Mater. Res. 1 (04) (1986) 601–609, http://dx.doi.org/10.1557/JMR.1986.0601.

[33] W.C. Oliver, G.M. Pharr, An improved technique for determining hardness and elastic modulus using load and displacement sensing indentation experiments, J. Mater. Res. 7 (6) (1992) 1564–1583, http://dx.doi.org/10.1557/JMR.1992.1564.

[34] A. Samadi-Dooki, G.Z. Voyiadjis, R.W. Stout, A combined experimental, modeling, and computational approach to interpret the viscoelastic response of the white matter brain tissue during indentation, J. Mech. Behav. Biomed. Mater. 77 (2018) 24–33, http://dx.doi.org/10.1016/j.jmbbm.2017.08.037, arXiv:28888930.

[35] E. Martynova, Determination of the properties of viscoelastic materials using spherical nanoindentation, Mech. Time-Depend. Mater. 20 (1) (2016) http://dx.doi.org/10.1007/s11043-015-9285-5.

[36] H. Lu, B. Wang, J. Ma, G. Huang, H. Viswanathan, Measurement of creep compliance of solid polymers by nanoindentation, Mech. Time-Depend. Mater. 7 (3) (2003) 189–207, http://dx.doi.org/10.1023/B:MTDM.0000007217.07156.9b.

[37] A. Jäger, R. Lackner, J. Eberhardsteiner, Identification of viscoelastic properties by means of nanoindentation taking the real tip geometry into account, Meccanica 42 (3) (2007) 293–306, http://dx.doi.org/10.1007/s11012-006-9041-7.

[38] R.F. Cook, A flexible model for instrumented indentation of viscoelastic–plastic materials, MRS Commun. 8 (2) (2018) 586–590, http://dx.doi.org/10.1557/mrc.2018.32.

[39] G. Peng, T. Zhang, Y. Feng, Y. Huan, Determination of shear creep compliance of linear viscoelastic–plastic solids by instrumented indentation, Polym. Test. 31 (8) (2012) 1038–1044, http://dx.doi.org/10.1016/j.polymertesting.2012.07.007.

[40] J. Menčík, L.H. He, M.V. Swain, Determination of viscoelastic–plastic material parameters of biomaterials by instrumented indentation, J. Mech. Behav. Biomed. Mater. 2 (4) (2009) 318–325, http://dx.doi.org/10.1016/j.jmbbm.2008.09.002.

[41] K.T. Kavanagh, R.W. Clough, Finite element applications in the characterization of elastic solids, Int. J. Solids Struct. 7 (1) (1971) 11–23, http://dx.doi.org/10.1016/0020-7683(71)90015-1.

[42] T. Nakamura, T. Wang, S. Sampath, Determination of properties of graded materials by inverse analysis and instrumented indentation, Acta Mater. 48 (17) (2000) 4293–4306, http://dx.doi.org/10.1016/s1359-6454(00)00217-2.

[43] Y. Gu, T. Nakamura, L. Prchlik, S. Sampath, J. Wallace, Micro-indentation and inverse analysis to characterize elastic–plastic graded materials, Mater. Sci. Eng. A 345 (1–2) (2003) 223–233, http://dx.doi.org/10.1016/s0921-5093(02)00462-8.

[44] G. Bolzon, G. Maier, M. Panico, Material model calibration by indentation, imprint mapping and inverse analysis, Int. J. Solids Struct. 41 (11–12) (2004) 2957–2975, http://dx.doi.org/10.1016/j.ijsolstr.2004.01.025.

[45] G. Rauchs, Optimization-based material parameter identification in indentation testing for finite strain elasto-plasticity, ZAMM Z. Angew. Math. Mech. 86 (7) (2006) 539–562, http://dx.doi.org/10.1002/zamm.200510261.

[46] G. Sun, F. Xu, G. Li, X. Huang, Q. Li, Determination of mechanical properties of the weld line by combining micro-indentation with inverse modeling, Comput. Mater. Sci. 85 (2014) 347–362, http://dx.doi.org/10.1016/j.commatsci.2014.01.006.

[47] Y. Fizi, Object-oriented finite element and inverse analysis to determine elastic–plastic properties of an arc-sprayed composite coating, in: A.F. de Mécanique (Ed.), CFM 2015-22ème Congrès Français de Mécanique, Congrès Français de Mécanique, AFM, Maison de la Mécanique, 39/41 rue Louis Blanc - 92400 Courbevoie, Lyon, France, 2015, colloque avec actes et comité de lecture. Internationale.

[48] A. Constantinescu, N. Tardieu, On the identification of elastoviscoplastic constitutive law from indentation tests, Inverse Prob. Eng. 9 (1) (2001) 19–44, http://dx.doi.org/10.1080/174159701088027751.

[49] M. Qasmi, P. Delobelle, F. Richard, C. Brun, M. Fromm, Viscoelastic mechanical properties determined by nanoindentation tests and its numerical modelling of polypropylene modified by He+ particle implantation and e(-) irradiation, Prog. Org. Coat. 51 (3) (2004) 195–204, http://dx.doi.org/10.1016/j.porgcoat.2004.07.012.

[50] R.R. Resapu, K.B. Nagendran, R.D. Bradshaw, A finite element method for the determination of optimal viscoelastic material properties from indentation tests of polymer film and wire with polymer insulation, Exp. Mech. 48 (6) (2008) 713–729, http://dx.doi.org/10.1007/s11340-007-9109-x.

[51] Y. Kucuk, C. Mollamahmutoglu, Y. Wang, H. Lu, Nonlinearly viscoelastic nanoindentation of PMMA under a spherical tip, Exp. Mech. 53 (5) (2013) 731–742, http://dx.doi.org/10.1007/s11340-012-9695-0.

[52] D.-L. Chen, P.-F. Yang, Y.-S. Lai, A review of three-dimensional viscoelastic models with an application to viscoelasticity characterization using nanoindentation, Microelectron. Reliab. 52 (3) (2012) 541–558, http://dx.doi.org/10.1016/j.microrel.2011.10.001.

[53] W. Yao, K. Yoshida, M. Fernandez, J. Vink, R.J. Wapner, C.V. Ananth, M.L. Oyen, K.M. Myers, Measuring the compressive viscoelastic mechanical properties of human cervical tissue using indentation, J. Mech. Behav. Biomed. Mater. 34 (2014) 18–26, http://dx.doi.org/10.1016/j.jmbbm.2014.01.016, arXiv:24548950.

[54] T.C. Ovaert, B.R. Kim, J. Wang, Multi-parameter models of the viscoelastic/plastic mechanical properties of coatings via combined nanoindentation and non-linear finite element modeling, Prog. Org. Coat. 47 (3) (2003) 312–323, http://dx.doi.org/10.1016/S0300-9440(03)00145-0.

[55] C. Poilâne, Z. Cherif, F. Richard, A. Vivet, B. Ben Doudou, J. Chen, Polymer reinforced by flax fibres as a viscoelastoplastic material, Compos. Struct. 112 (2014) 100–112, http://dx.doi.org/10.1016/j.compstruct.2014.01.043.

[56] X. Shi, S. Jiang, L. Yang, M. Tang, D. Xiao, Modeling the viscoelasticity of shale by nanoindentation creep tests, Int. J. Rock Mech. Min. Sci. 127 (2020) 104210, http://dx.doi.org/10.1016/j.ijrmms.2020.104210.

[57] Z. Wu, T.A. Baker, T.C. Ovaert, G.L. Niebur, The effect of holding time on nanoindentation measurements of creep in bone, J. Biomech. 44 (6) (2011) 1066–1072, http://dx.doi.org/10.1016/j.jbiomech.2011.01.039.

[58] Y. Kucuk, C. Mollamahmutoglu, Y. Wang, H. Lu, Nonlinearly viscoelastic nanoindentation of PMMA under a spherical tip, Exp. Mech. 53 (5) (2013) 731–742, http://dx.doi.org/10.1007/s11340-012-9695-0.

[59] K. Liu, M.R. VanLandingham, T.C. Ovaert, Mechanical characterization of soft viscoelastic gels via indentation and optimization-based inverse finite element analysis, J. Mech. Behav. Biomed. Mater. 2 (4) (2009) 355–363, http://dx.doi.org/10.1016/j.jmbbm.2008.12.001.

[60] X. Hou, N. Jennett, Defining the limits to long-term nano-indentation creep measurement of viscoelastic materials, Polym. Test. 70 (2018) 297–309, http://dx.doi.org/10.1016/j.polymertesting.2018.07.022.

[61] Z. Chen, S. Diebels, N.J. Peter, A.S. Schneider, Identification of finite viscoelasticity and adhesion effects in nanoindentation of a soft polymer by inverse method, Comput. Mater. Sci. 72 (2013) 127–139, http://dx.doi.org/10.1016/j.commatsci.2013.01.040.

[62] F. Richard, M. Villars, S. Thibaud, Viscoelastic modeling and quantitative experimental characterization of normal and osteoarthritic human articular cartilage using indentation, J. Mech. Behav. Biomed. Mater. 24 (2013) 41–52, arXiv:23684353.

[63] D.S. Simulia, Abaqus user's guide.

[64] A. Plunkett, K. Temiz, C. Warren, V. Wisniewski, K.P. Furlan, J. Garay, D. Giuntini, B. Domènech, G.A. Schneider, Bridging nanocrystals to robust, multifunctional, bulk materials through nature-inspired, hierarchical design, 2022, http://dx.doi.org/10.26434/chemrxiv-2022-mxtm4.

[65] X.W. Gu, X. Ye, D.M. Koshy, S. Vachhani, P. Hosemann, A.P. Alivisatos, Tolerance to structural disorder and tunable mechanical behavior in self-assembled superlattices of polymer-grafted nanocrystals, Proc. Natl. Acad. Sci. 114 (11) (2017) 2836–2841, http://dx.doi.org/10.1073/pnas.1618508114.

[66] G. Huang, H. Lu, Measurement of young's relaxation modulus using nanoindentation, Mech. Time-Depend. Mater. 10 (3) (2006) 229–243, http://dx.doi.org/10.1007/s11043-006-9020-3.

[67] M. Sebastiani, K. Johanns, E. Herbert, G. Pharr, Measurement of fracture toughness by nanoindentation methods: Recent advances and future challenges, Curr. Opin. Solid State Mater. Sci. 19 (6) (2015) 324–333, http://dx.doi.org/10.1016/j.cossms.2015.04.003.

[68] J. Dean, T. Clyne, Extraction of plasticity parameters from a single test using a spherical indenter and FEM modelling, Mech. Mater. 105 (2017) 112–122, http://dx.doi.org/10.1016/j.mechmat.2016.11.014.

[69] B.N. Lucas, W.C. Oliver, Indentation power-law creep of high-purity indium, Metall. Mater. Trans. A 30 (3) (1999) 601–610, http://dx.doi.org/10.1007/s11661-999-0051-7.

[70] Z.C. Duan, A.M. Hodge, High-temperature nanoindentation: New developments and ongoing challenges, JOM 61 (12) (2009) 32–36, http://dx.doi.org/10.1007/s11837-009-0177-5.

[71] N. Everitt, M. Davies, J. Smith, High temperature nanoindentation – the importance of isothermal contact, Phil. Mag. 91 (7–9) (2011) 1221–1244, http://dx.doi.org/10.1080/14786435.2010.496745.

[72] S. Korte, R.J. Stearn, J.M. Wheeler, W.J. Clegg, High temperature microcompression and nanoindentation in vacuum, J. Mater. Res. 27 (1) (2011) 167–176, http://dx.doi.org/10.1557/jmr.2011.268.

[73] Y.C. Lu, D.C. Jones, G.P. Tandon, S. Putthanarat, G.A. Schoeppner, High temperature nanoindentation of pmr-15 polyimide, Exp. Mech. 50 (4) (2009) 491–499, http://dx.doi.org/10.1007/s11340-009-9254-5.

[74] V. Maier, B. Merle, M. Göken, K. Durst, An improved long-term nanoindentation creep testing approach for studying the local deformation processes in nanocrystalline metals at room and elevated temperatures, J. Mater. Res. 28 (9) (2013) 1177–1188, http://dx.doi.org/10.1557/jmr.2013.39.

[75] I.N. Sneddon, The relation between load and penetration in the axisymmetric boussinesq problem for a punch of arbitrary profile, Internat. J. Engrg. Sci. 3 (1) (1965) 47–57, http://dx.doi.org/10.1016/0020-7225(65)90019-4.

[76] X.W. Gu, Mechanical properties of architected nanomaterials made from organic–inorganic nanocrystals, JOM 70 (10) (2018) 2205–2217, http://dx.doi.org/10.1007/s11837-018-3094-7.

[77] M.-P. Pileni, Mechanical properties of supracrystals, Europhys. Lett. 119 (3) (2017) 37002, http://dx.doi.org/10.1209/0295-5075/119/37002.

[78] P. Parakala, R.A. Mirshams, S. Nasrazadani, K. Lian, Effects of thickness and indenter geometry in nanoindentation of nickel thin films, MRS Proc. 795 (2003) http://dx.doi.org/10.1557/proc-795-u11.19.

[79] J. Hurtado, I. Lapczyk, S. Govindarajan, Parallel rheological framework to model non-linear viscoelasticity, permanent set and mullins effect in elastomers, in: Book - Constitutive Models for Rubber VIII, 2013, pp. 95–100, http://dx.doi.org/10.1201/b14964-21.

[80] B. Hoddy, N. Ahmed, K. Al-lamee, N. Bullett, N.W. Bressloff, Exploring a parallel rheological framework to capture the mechanical behaviour of a thin-strut polymeric bioresorbable coronary scaffold, J. Mech. Behav. Biomed. Mater. 130 (2022) 105154, http://dx.doi.org/10.1016/j.jmbbm.2022.105154.

[81] H.S. Aldhufairi, O. Olatunbosun, K. Essa, Determination of a tyre's rolling resistance using parallel rheological framework, in: SAE Technical Paper Series, SAE International, 2019, http://dx.doi.org/10.4271/2019-01-5069.

[82] A. Chakraborty, P. Eisenlohr, Evaluation of an inverse methodology for estimating constitutive parameters in face-centered cubic materials from single crystal indentations, Eur. J. Mech. A Solids 66 (2017) 114–124, http://dx.doi.org/10.1016/j.euromechsol.2017.06.012.

[83] J. Campbell, R. Thompson, J. Dean, T. Clyne, Experimental and computational issues for automated extraction of plasticity parameters from spherical indentation, Mech. Mater. 124 (2018) 118–131, http://dx.doi.org/10.1016/j.mechmat.2018.06.004.

[84] J. Campbell, R. Thompson, J. Dean, T. Clyne, Comparison between stress–strain plots obtained from indentation plastometry, based on residual indent profiles, and from uniaxial testing, Acta Mater. 168 (2019) 87–99, http://dx.doi.org/10.1016/j.actamat.2019.02.006.

[85] J.K. Engels, N. Vajragupta, A. Hartmaier, Parameterization of a non-local crystal plasticity model for tempered lath martensite using nanoindentation and inverse method, Front. Mater. 6 (2019) http://dx.doi.org/10.3389/fmats.2019.00247.

[86] H. Liu, J. Ma, A. Tang, J. Tang, C. Zhang, L. Zhang, Y. Shen, True stress–strain curvfe extraction from ion-irradiated materials via small tensile, small punch and nanoindentation tests: method development and accuracy/consistency verification, Nucl. Fusion 60 (5) (2020) 056012, http://dx.doi.org/10.1088/1741-4326/ab7c2a.

[87] https://polymerfem.com/mcalibration/, Mcalibration user's guide.

[88] E.G. Herbert, P.S. Phani, K.E. Johanns, Nanoindentation of viscoelastic solids: A critical assessment of experimental methods, Curr. Opin. Solid State Mater. Sci. 19 (6) (2015) 334–339, http://dx.doi.org/10.1016/j.cossms.2014.12.006.

[89] B. Merle, V. Maier-Kiener, G.M. Pharr, Influence of modulus-to-hardness ratio and harmonic parameters on continuous stiffness measurement during nanoindentation, Acta Mater. 134 (2017) 167–176, http://dx.doi.org/10.1016/j.actamat.2017.05.036.

[90] J.A. Wahlquist, F.W. DelRio, M.A. Randolph, A.H. Aziz, C.M. Heveran, S.J. Bryant, C.P. Neu, V.L. Ferguson, Indentation mapping revealed poroelastic, but not viscoelastic, properties spanning native zonal articular cartilage, Acta Biomater. 64 (2017) 41–49, http://dx.doi.org/10.1016/j.actbio.2017.10.003.

[91] Y. Shelef, B. Bar-On, Size effects on the dynamic indentation modulus of films, Mech. Mater. 164 (2022) 104118, http://dx.doi.org/10.1016/j.mechmat.2021.104118.